Strain-driven formation of rubrene crystalline films on Bi(001)

Meng Lan, Zu-Hong Xiong, Guo-Qing Li, Ting-Na Shao, Jia-Le Xie, Xiu-Fan Yang, Jun-Zhong Wang, and Ying Liu

Phys. Rev. B **83**, 195322 — Published 25 May 2011

DOI: 10.1103/PhysRevB.83.195322

Strain-driven Formation of Rubrene Crystalline Films on Bi(001)

Meng Lan,[1] Zu-Hong Xiong,[1] Guo-Qing Li,[1]Ting-Na Shao,[1] Jia-Le Xie,[1] Xiu-Fan Yang,[1] Jun-Zhong Wang,[1, *] and Ying Liu[2, *]

[1] *School of Physical Science and Technology & MOE Key Laboratory on Luminescence and Real-Time Analysis, Southwest University, Chongqing 400715, P. R. China*

[2] *Department of Physics and Hebei Advanced Thin Film Laboratory, Hebei Normal University, Shijiazhuang 050016, Hebei, P. R. China*

Abstract

We report the formation of rubrene crystalline films on Bi(001) substrate starting from the very first layer. With coverage increasing, rubrene shows a structural evolution from self-assembled monolayer to a composite phase, which consists of rubrene crystalline domains and self-assembled domain walls. In particular, Kurdjunov-Sachs (KS) rotational epitaxy has been found in rubrene crystalline domains, which reveal large compressive strains. Further deposition of rubrene leads to a layer-by-layer growth of crystalline films up to the forth layer. The driving force for rubrene crystallinity in monolayer regime has been attributed to the anisotropic strains generated in KS rotation epitaxy.

PACS number: 68.55.am, 61.66.Hq, 68.35.bm, 68.37.Ef

---

[*] E-mail: jzwangcn@swu.edu.cn; yliu@hebtu.edu.cn

I. Introduction

Organic semiconductor has significant applications in microelectronic devices such as organic light emitting diodes (OLEDs) and organic field effect transistors (OFETs).[1-5] Since charge transports depend strongly on the lateral ordering and crystallinity degree at the molecule/substrate interface, it is necessary to fabricate organic crystalline films starting from the first monolayer. However, as most organic molecules exhibit shape anisotropy and additional degrees of freedom, the molecular orientation and conformation may change during growth, introducing additional sources of disorder.

Rubrene ($C_{42}H_{28}$), comprised of a tetracene backbone and four phenyl side groups, has been recently identified as a promising material due to the efficient luminescence and high charge carrier mobility. OFETs made of rubrene single crystals reveal a very high carrier mobility (~15 cm^2/Vs).[6, 7] Nevertheless, it is difficult to produce rubrene-based OFETs with satisfactory electronic properties, due to the inablility in growing rubrene epitaxial films by organic molecular beam deposition (OMBD). Käfer *et al.* studied the fundamental mechanism that limits the epitaxy growth of rubrene.[8] They demonstrated that the tetracene backbones of rubrene molecules remains twisted upon deposition of first few monolayers, whereas it becomes planar at higher coverage. As a consequence, the first monolayers of rubrene are disordered, hindering further formation of crystalline films. Density function theory (DFT) calculations reveal that the free rubrene molecule has a twisted (~ 42°) tetracene backbone, leading to an axial chirality as shown in Fig. 1(a), while the rubrene crystals adopt a planar tetracene backbone without any chirality.[9]

Recently there has been tremendous effort in growing rubrene crystalline thin films on various substrates. Nevertheless, a lot of self-assembled monolayer (SAM) or supramolecular structures have been obtained on noble-metal substrates like Au,[10-14] Cu, [9, 15, 16] and Ag.[17] For thick rubrene films, amorphous or polycrystalline rubrene films formed upon deposition onto muscovite,[18], SiO_2 without [19] or with buffer layers.[20, 21] Multilayer rubrene islands with a rectangular lattice distinct from the *a*-*b* plane of rubrene crystal have been found on Au(111).[22] In particular, thick rubrene films with crystalline orientation have been obtained by special solution processing[23] or by hot wall deposition on Au(111).[24] AFM measurements indicated a step height close to the *d*-spacing of *a*-*b* plane in rubrene crystals. However, it is

not clear about the in-plane structure as well as the crystallinity degree near molecule/substrate interface. Thus growth of rubrene crystalline films on appropriate substrates starting from the first monolayer remains still a big challenge.

It was reported recently that pentacene, another benchmark molecule, grown on the semi-metallic Bi(001) substrate forms the epitaxial crystalline films with pentacene molecule standing-up, even in the first monolayer.[25, 26] The upright orientation of pentacene molecule is attributed to the small density of states near Fermi level, which leads to the reduction of molecule-substrate interaction.[27] In this letter, we demonstrate the formation of rubrene crystalline films on Bi(001) starting from the molecule/substrate interface. A composite phase consisting of rubrene crystalline domains and self-assembled domain walls has been observed in the first monolayer. Afterwards, the layer-by-layer growth of rubrene crystalline films has been found to persist up to the forth monolayer. The crystallinity of rubrene molecules in monolayer regime has been attributed to the large strains resulting from Kurdjunov-Sachs (KS) rotation epitaxy.[28, 29]

II. Experiments

The experiments were performed in an ultrahigh vacuum low temperature STM (Unisoku) with the base pressure ~1.2×10^{-10} mbar. Bi(001) thin film was prepared by depositing 20 ML Bi on Si(111)-7x7 at room temperature (RT) with subsequent annealing at ~120ºC. Rubrene molecules (Aldrich, purity 99%) were grown at RT from a quartz Knudsen cell heated to ~ 200 ºC. The typical growth rate was about 0.03 ML per minute. Through this paper we define rubrene coverage in term of crystalline monolayer (ML) corresponding to the *a*-*b* plane in rubrene crystals. In order to establish the adsorption model of rubrene molecule, spin-polarized DFT geometric optimization with the generalized gradient approximation (GGA) has been performed. The gradient corrected Perdew-Wang 91 exchange-correlation functional and double-numerical polarized basis were employed.[30] Fig. 1(b) shows the side view of the optimized geometry of a rubrene molecule adsorbed on Bi(001) surface, where the long axis of tetracene backbone exhibit a 29.8° angle with respect to the substrate plane, and the closest molecule-substrate distance is 2.5 Å. Fig. 1(c) is the top view of calculated total electronic density of rubrene molecule. It is consistent with the experimental STM image

displayed in Fig. 1(d), where rubrene molecule reveals five protrusions.

III. Experimental Results

When deposited on Bi(001), rubrene molecules are initially self-assembled into monolayer islands, which prefer to stick the step edges of Bi substrate, Fig. 2(a). On the complete layer of rubrene SAM, a Moiré pattern characterized by a 4 × 3 super-cell has been observed, Fig. 2(b). The lattice constants of rubrene SAM are c_1 = 14.6 ± 0.2 Å, c_2 = 16.6 ± 0.2 Å, θ = 68.0 ± 0.5°, and c_1 is parallel to a principal axis of Bi(001). The packing density is calculated to be ~0.89 nm^{-2}. Based on the Moiré pattern and the lattice constant of Bi(001) surface ($a_1 = a_2$ = 4.54 Å),[31] the SAM lattice vectors can be expressed as:

$$\begin{pmatrix} c_1 \\ c_2 \end{pmatrix} = \begin{pmatrix} 13/4 & 0 \\ -2/3 & 4 \end{pmatrix} \begin{pmatrix} a_1 \\ a_2 \end{pmatrix} \qquad (1)$$

The presence of two integers in the single column of transformation matrix, reveals a point-on-line coincident relation between rubrene SAM and Bi(001).[32] From the high-resolution STM image in Figure 2(c), we noticed that each unit cell includes two in-equivalent molecules: one manifests three protrusions similar to the molecular image in supramolecular structures; [10] the other exhibits five protrusion lobes, similar to the molecular image appeared in Fig. 1(d). Thus we speculate that each molecule in rubrene SAM adopt an essentially lying-down orientation on Bi(001). Fig. 2(d) is the schematic diagram for the structural model of rubrene SAM, where all the molecular lattice points reside on the substrate lattice lines along a_2-axis (point-on-line).

Upon further increasing the rubrene coverage, it is found that rubrene SAM transforms into a composite phase, which corresponds to a collection of rubrene crystalline domains separated by domain walls. Fig. 3(a) shows the derivative of topographic STM image for rubrene composite phase, in order to enhance the appearance of surface features. It is noticed that the domain walls exhibit zigzag patterns with parallel alignments. From the close-up view in Fig. 3(b), we noticed that the domain walls are aligned along either $[\bar{1}\,\bar{1}\,2]$ or $[1\,\bar{2}\,1]$ direction of Bi(001). From the high-resolution STM image in Fig. 3(c), it is observed that the domain walls have a hexagonal lattice (c = 15.5 ± 0.1 Å), which is $2\sqrt{3} \times 2\sqrt{3}$ reconstructed with Bi(001). Within the crystalline domains, a rectangular lattice with herringbone molecule

packing has been identified. The lattice constants are a = 12.6 ± 0.1 Å, b = 7.3 ± 0.1 Å, very close to those of the a-b plane in rubrene crystals (a_0 = 14.4 Å, b_0 = 7.2 Å [33]). Thus this rubrene crystalline phase corresponds to a strained a-b plane of rubrene crystal. The molecular packing density is 2.2 nm^{-2}, which is 2.5 times of that in rubrene SAM. By calculating the transformation matrix, we realized that this crystalline phase is incommensurate with Bi(001). We noticed that this crystalline phase exhibits the similar in-plane structure as the thick crystalline films of rubrene obtained by solution processing[23] or hot wall deposition.[24] However, their crystallization ways are different. our crystalline rubrene phase formed in the monolayer regime; while it is not clear about the crystallinity degree near the molecule/substrate interface for thick crystalline films mentioned above. Here we define the anisotropic strain as the fractional deviation of each lattice constant from the bulk value, thus $\delta_a = (a - a_0) / a_0 = -12.5$ %, $\delta_b = (b - b_0) / b_0 = 1.4$ %. It means that a large compressive strain builds up in the rubrene crystalline phase. Furthermore, this strain is highly anisotropic ($\delta_a >> \delta_b$). In addition, we noticed that one c-axis of the domain walls is parallel to the a-axis of crystalline phase, while the a-axis and b-axis of crystalline phase are parallel to $[\bar{1}01]$ and $[1\bar{2}1]$ directions of Bi(001), respectively. The structural model for rubrene composite phase is shown in Fig. 3(d). Interestingly, it is observed that a and b axes constitute a "right-angle triangle with an angle of 30.1°, which matches precisely with the hexagonal lattice of Bi(001). Thus we can say the lattice alignment of rubrene crystalline phase is "locked-in" by the hexagonal lattice of Bi(001) in spite of the incommensurism.

In fact, a similar orientational relationship was found in bcc(110)/fcc(111) system.[28, 29, 34] In Nishiyama-Wassermann (NW) orientation, the b-axis of bcc(110) is parallel to a principal axis of fcc(111) lattice, Fig. 3(e). If rubrene crystalline phase adopts this orientation, the lattice misfit would be m_{NW} = 19.8 %, which is too large to be favored. In the KS orientation, the fcc(111) lattice rotates an angle of 30° such that the a-axis of bcc(110) is parallel to a principal axis of fcc (111), Fig. 3(f). If rubrene crystalline phase adopts KS orientation, the lattice misfit will reduce significantly to m_{KS} = 7.4 %. Coincidently, we realized that the structural model of rubrene crystalline phase shown in Fig. 3(d), is consistent with KS orientation. According to the analysis by Zangwill,[29] in KS rotational epitaxy, the incommensurate film achieves row matching only in an average sense. Coherence is lost

through a complicate interplay of domain walls along one direction, and non-uniform strains in the other. This prediction is in agreement with our observation in rubrene composite phase.

On the other hand, it seems that the formation of crystalline rubrene layer in the first layer is surprising, since DFT calculation revealed that energy difference between the twisted rubrene molecules in gas (or in thin films) and the planar molecules in crystals is 205 meV.[9] This means that, in order to realize the crystallinity of rubrene molecules in monolayer regime, it requires additional energy ~205 meV to stabilize the planarization of twisted backbone of rubrene molecule. One may ask where this energy comes from? The building up of large compressive strain in rubrene crystalline phase, reminds us that this additional energy comes from the elastic strain energy generated in KS rotational epitaxy.

Upon further deposition of rubrene, layer-by-layer growth of rubrene crystalline layers has been observed. Fig. 4(b) shows a second layer island of crystalline rubrene crossing several terraces. From the linescan shown in Fig. 4(a), we can distinguish the ~1.3 nm step height associated with the *d*-spacing of *a*-*b* plane in rubrene crystals (1.35 nm), as well as the ~0.4 nm step height of Bi(001) (the same as step height of rubrene composite phase due to the uniform covering). Fig. 4(c) shows the morphology of continuous second layer formed at ~1.6 ML. It is found that the morphology second rubrene layer is very smooth. In order to verify the two-dimensional growth mode, we scanned many places of the second rubrene layer. All of them exhibit the same lattice structure with same orientation. Furthermore, we have also performed atomic force microscopy (AFM) scanning (~15 μm) on the different regions of sample surface. All the AFM images reveal smooth morphology of second rubrene layer, no three-dimensional rubrene island and domain boundary have been found. Fig. 4(d) and Fig. 4(e) show the bias-dependent STM images with sub-molecular resolution acquired on the second rubrene layer, where the top two phenyl side groups of rubrene molecule can be resolved. Compared with the crystalline rubrene in the first layer, the lattice constant for second rubrene layer reveal some modification: $a' = 13.8 \pm 0.1$ Å, $b' = 7.1 \pm 0.1$ Å. The anisotropic strains are reduced to $\delta'_a = -4.2$ %, $\delta'_b = -1.4$ %. Most importantly, we noticed a "lattice rotation" for the second rubrene layer: the a'-axis of second rubrene layer deviates the principal axis of Bi(001) for a small angle (~5°). Thus we conclude that the lattice rotation of second rubrene layer leads to a significant relief of strain. When the rubrene coverage is

increased to 4 ML, we found a transition from two-dimensional to three-dimensional growth, corresponding to Stranski-Krastanov mode. However, due to the poor conductivity of multilayer rubrene, STM scanning becomes difficult even at very small tunneling current. In order to avoid the imaging artifacts, we perform tapping mode AFM measurements for 4 ML of rubrene films, Fig. 4(f). It is found the morphology of the multilayer rubrene is essentially smooth, except some facet islands revealed by the bright protrusions. For higher coverage of rubrene films, AFM observation indicates that the film morphology becomes very rough.

IV. Conclusion

To summarize, crystalline rubrene films formed on the semi-metallic Bi(001) substrate, even from the first monolayer. A composite phase consisting of rubrene crystalline domains and self-assembled domain walls, appeared in the first rubrene layer. Most importantly, KS rotational epitaxy has been found in the rubrene crystalline domains. Further deposition of rubrene leads to a layer-by-layer growth of rubrene crystalline films up to the forth layer. The driving force for rubrene crystallinity in monolayer regime can be attributed to the large compressive strains resulting from KS rotation epitaxy.

V. Acknowledgement

This work was supported by the National Natural Science Foundation of China (Grant No. 10974156), and Natural Science Foundation Project of CQ CSTC (Grant No. 2008BB4003).

VI. References

1. V. C. Sundar, J. Zaumseil, V. Podzorov, E. Menard, R. L. Willett, T. Someya, M. E. Gershenson, and J. A. Rogers, Science **303**, 1644 (2004).
2. F.-J. M. z. Heringdorf, M. C. Reuter, and R. M. Tromp, Nature **412**, 517 (2001).
3. G. Witte and C. Wöll, Phys. Stat. Sol. **205**, 497 (2008).
4. F. Schreiber, Phys. Stat. Sol. **201**, 1037 (2004).
5. G. Witte and C. Wöll, J. Mater. Res. **19**, 1889 (2004).
6. V. Podzorov, E. Menard, A. Borissov, V. Kiryukhin, J. A. Rogers, and M. E. Gershenson, Phys. Rev. Lett. 93, 086602 (2004).
7. R. Zeis, C. Besnard, T. Siegrist, C. Schlockmann, X. Chi, and C. Kloc, Chem. Mater. 18, 244 (2006).
8. D. Käfer, L. Ruppel, G. Witte, and C. Wöll, Phys. Rev. Lett. **95**, 166602 (2005).

9. J. A. Miwa, F. Cicoira, S. Bedwani, J. Lipton-Duffin, D. F. Perepichka, A. Rochefort, and F. Rosei, J. Phys. Chem. C **112**, 10214 (2008).
10. M. C. Blüm, E. Cavar, M. Pivetta, F. Patthey, and W. D. Schneider, Angew. Chem. Int. Edit. **117**, 5468 (2005).
11. M. Pivetta, M. C. Blüm, F. Patthey, and W. D. Schneider, Angew. Chem. Int. Edit. **120**, 1092 (2008).
12. M. C. Blüm, M. Pivetta, F. Patthey, and W. D. Schneider, Phys. Rev. B **73**, 195409 (2006).
13. L. Wang, S. Chen, L. Liu, D. Qi, X. Gao, and A. T. S. Wee, Appl. Phys. Lett. **90**, 132121 (2007).
14. L. Wang, H. Kong, X. Chen, X. Du, F. Chen, X. Liu, and H. Wang, Appl. Phys. Lett. **95**, 093102 (2009).
15. F. Cicoira, J. A. Miwa, D. F. Perepichka, and F. Rosei, J. Phys. Chem. A **111**, 12674 (2007).
16. J. A. Miwa, F. Cicoira, J. Lipton-Duffin, D. F. Perepichka, C. Santato, and F. Rosei, Nanotechnology **19**, 424021 (2008).
17. M. Pivetta, M. C. Blüm, F. Patthey, and W. D. Schneider, ChemPhysChem **11**, 1558 (2010).
18. T. Djuric, A. Thierry, W. Grogger, S. M. AbdAl-Baqi, H. Sitter, and R. Resel, Physica E **41**, 1718 (2009).
19. S. Kowarik, A. Gerlach, S. Sellner, F. Schreiber, J. Pflaum, L. Cavalcantid, and O. Konovalovd, Phys. Chem. Chem. Phys. **8**, 1834 (2006).
20. W. S. Hu, S. Z. Weng, Y. T. Tao, H. J. Liu, and H. Y. Lee, Org. Electron. **9**, 385 (2008).
21. C. H. Hsu, J. Deng, C. R. Staddon, and P. H. Betona, Appl. Phys. Lett. **91**, 193505 (2007).
22. M. Pivetta, M. C. Blum, F. Patthey, and W. D. Schneider, J. Phys. Chem. B **113**, 4578 (2009).
23. N. Stingelin-Stutzmann, E. Smits, H. Wondergem, C. Tanase, P. Blom, P. Smith, and D. Deleeuw, Nature Mater. **4**, 601 (2005).
24. D. Käfer and G. Witte, Phys. Chem. Chem. Phys. **7**, 2850 (2005).
25. J. T. Sadowski, T. Nagao, S. Yaginuma, Y. Fujikawa, A. Al-Mahboob, K. Nakajima, T. Sakurai, G. E. Thayer, and R. M. Tromp, Appl. Phys. Lett. **86**, 073109 (2005).
26. G. E. Thayer, J. T. Sadowski, F. M. z. Heringdorf, T. Sakurai, and R. M. Tromp, Phys. Rev. Lett. **95**, 256106 (2005).
27. H. Kakuta, T. Hirahara, I. Matsuda, T. Nagao, S. Hasegawa, N. Ueno, and K. Sakamoto, Phys. Rev. Lett. **98**, 247601 (2007).
28. E. Bauer and J. H. vanderMerwe, Phys. Rev. B **33**, 3657 (1986).
29. A. Zangwill, *Physics at Surface* (Cambridge University Press, Cambridge, 1988).
30. J. P. Perdew and Y. Wang, Phys. Rev. B **45**, 13244 (1992).
31. T. Nagao, *et al*., Phys. Rev. Lett. **93**, 105501 (2004).
32. D. E. Hooks, T. Fritz, and M. D. Ward, Adv. Mater. **13**, 227 (2001).
33. D. E. Henn, W. G. Williams, and D. J. Gibbson, J. Appl. Cryst. **4**, 256 (1971).
34. A. D. Novaco and J. P. McTague, Phys. Rev. Lett. **38**, 1286 (1977).

Figure captions:

FIG. 1. (color online). (a) Schematic structure of the free rubrene molecule. (b) Side view of the optimized adsorption model of rubrene on Bi(001). The atoms within top two layers of Bi substrate are labeled by different colors. (c) Top view of the calculated total electron density for the optimized rubrene molecule. (d) STM image of singular rubrene molecule adsorbed on Bi(001), 3 nm × 3 nm, 2.0 V.

FIG. 2. (color online). STM images for the self-assembled monolayer (SAM) of rubrene formed on Bi(001). (a) A self-assembled rubrene island sticking to the step edges of substrate, 135 nm × 135 nm, 2.0 V. Insert is atomic-resolution STM image of Bi(001) surface. (b) The SAM of rubrene formed at ~0.4 ML, with a Moiré pattern characterized by 4 × 3 super-cell, 20 nm × 20 nm, 2.5 V. (c) High-resolution STM image acquired on the rubrene SAM, 10 nm × 10 nm, 3.5 V. (d) Schematic diagram for the point-on-line coincidence orientation of rubrene SAM on Bi(001).

FIG. 3. (color online). Rubrene composite phase formed on Bi(001) at ~0.7 ML. (a) Derivative of the topographic STM image for the rubrene composite phase, 100 nm × 100 nm, 4.5 V. (b) STM image of rubrene composite phase, shows clearly the alignments of domain walls, 25 nm × 25 nm, 2.5 V. (c) High-resolution STM image of the rubrene composite phase, 9 nm × 9 nm, 2.5 V. (d) Schematic illustration for the structural model of rubrene composite structure. (e) and (f) show the Nishiyama-Wassermann (NW) and Kurdjumov-Sachs (KS) orientation relationships between the quasi-bcc(110) lattice of crystalline rubrene and fcc(111) substrate, respectively.

FIG. 4. (color online). Subsequent layer-by-layer growth of rubrene crystalline layers on top of the composite phase. (a) Linescan corresponding to the blue line shown in (b). (b) STM image of a second layer rubrene island, 500 nm × 500 nm, 4.5 V. (c) STM image of the continuous second layer of rubrene formed at ~1.5 ML, 500 nm × 500 nm, 4.5 V. (d) and (e) are the high-resolution STM images acquired on the rubrene second layer with the bias of –4.0 V,

and −2.0 V, respectively. The blue arrow is used to mark the direction of a principal axis of Bi(001), 6 nm × 6 nm. (f) Tapping-mode AFM image of the rubrene films with ~ 4 ML thickness, 14 μm × 14 μm.

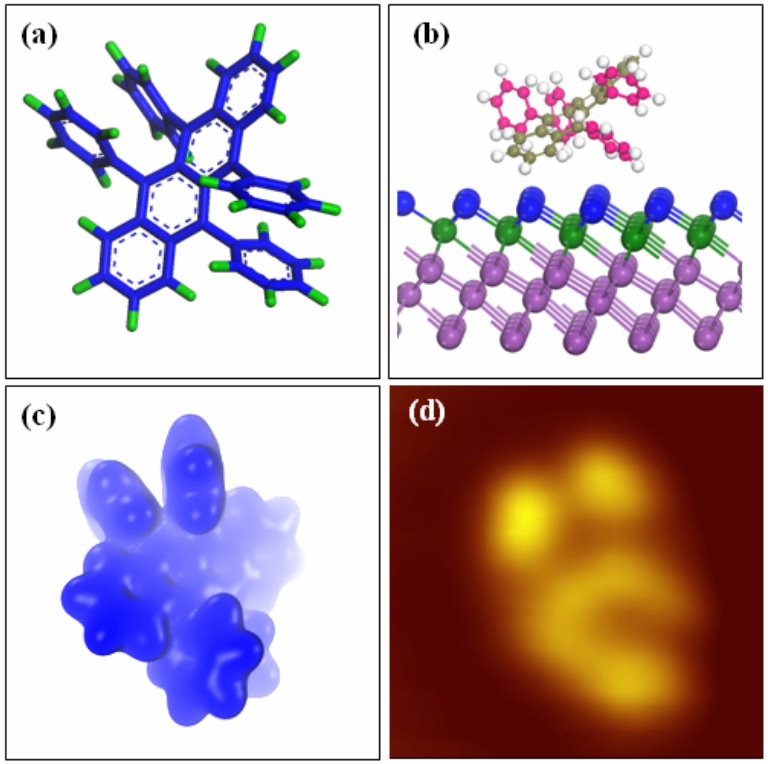

Lan *et al*., Figure 1

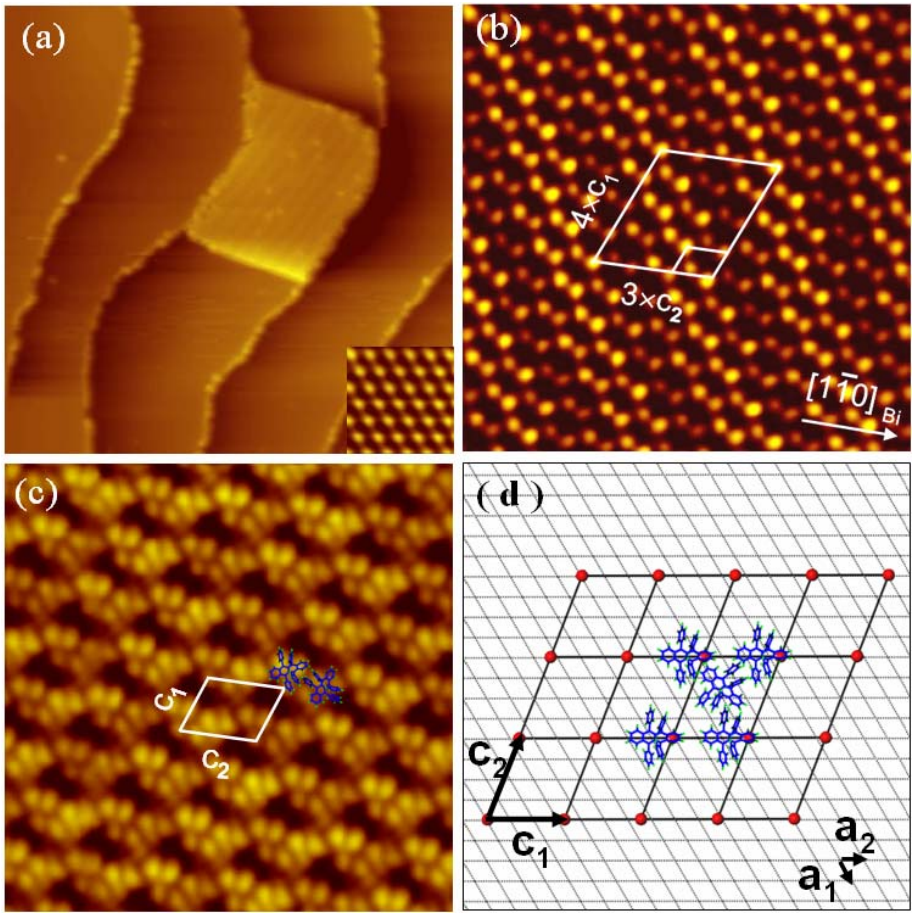

Lan *et al*., Figure 2

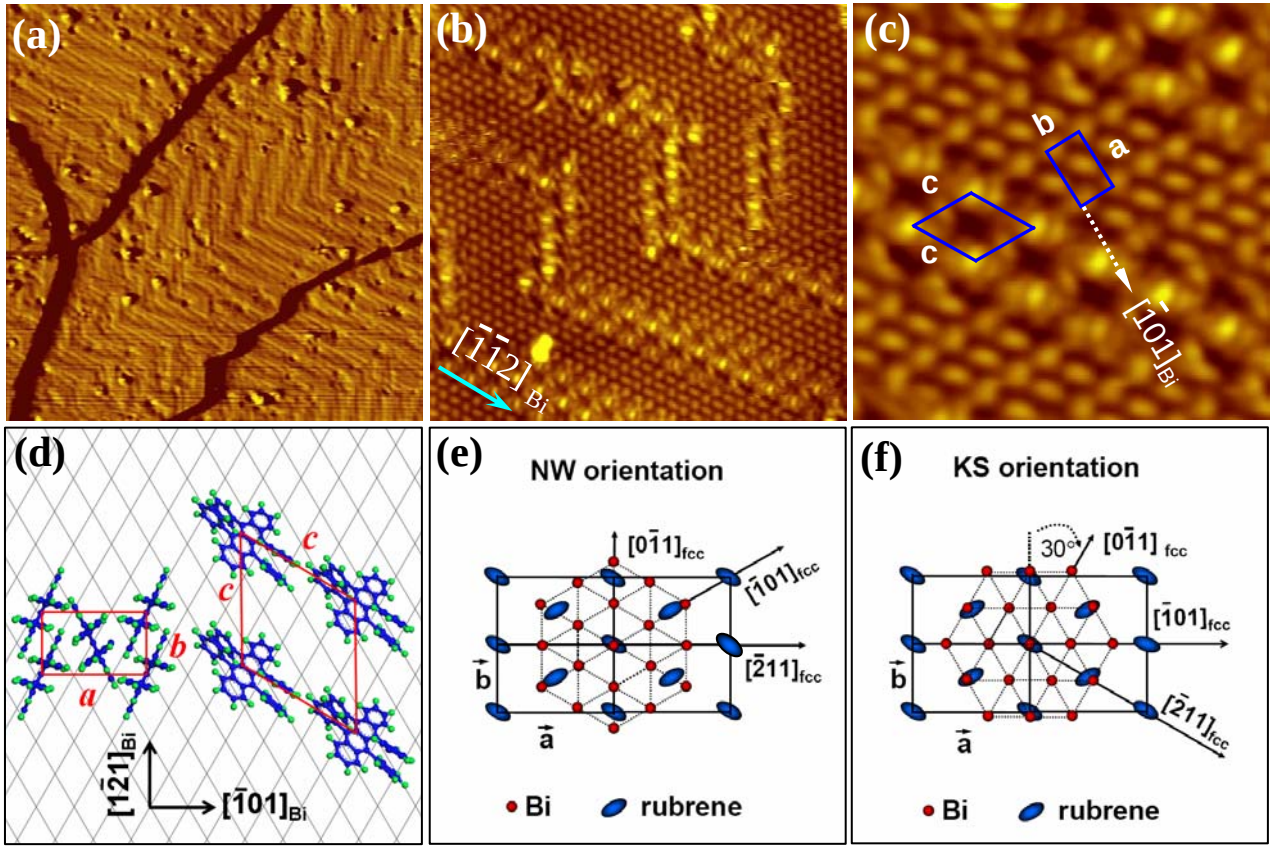

Lan *et al*., Figure 3

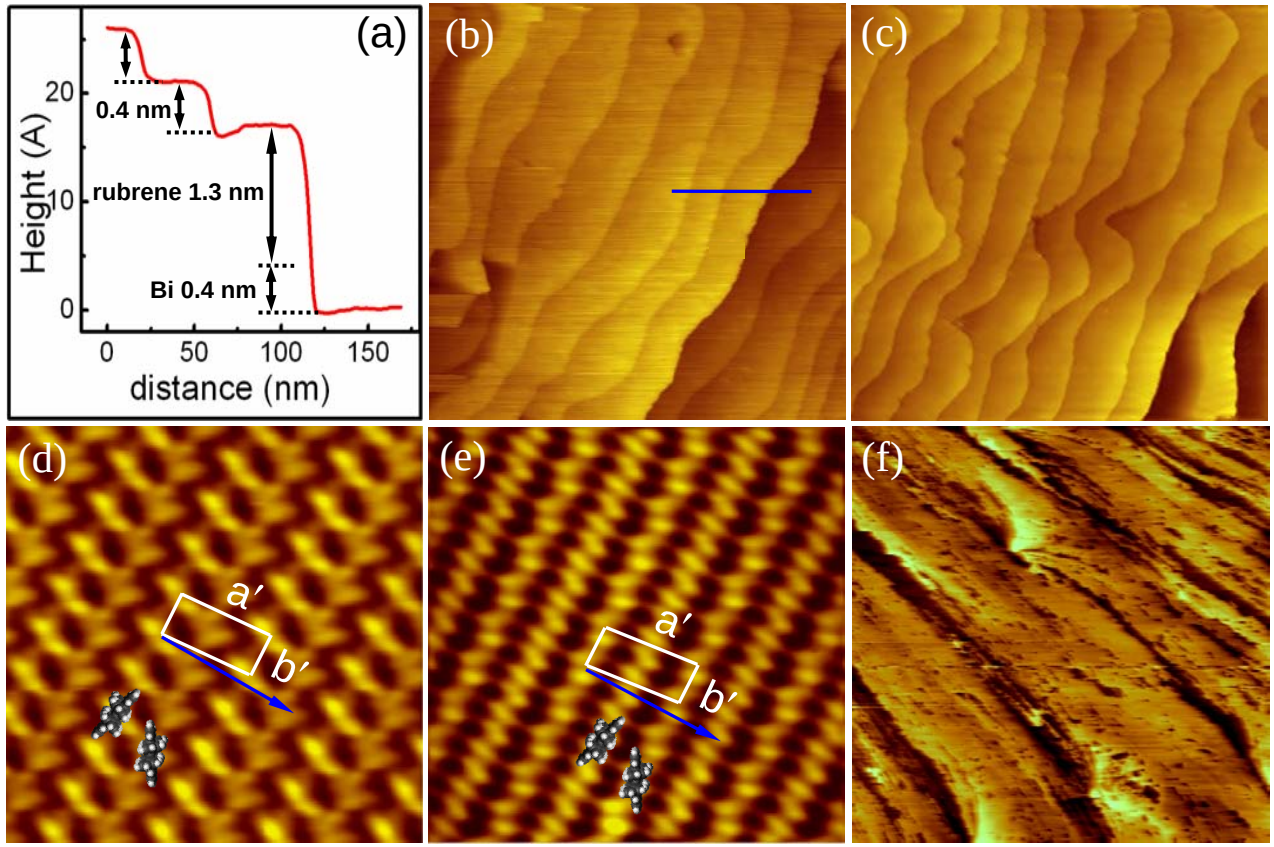

Lan *et al*., Figure 4